

Inducing Ferrimagnetism in Insulating Hollandite $\text{Ba}_{1.2}\text{Mn}_8\text{O}_{16}$

Amber M. Larson,[†] Pouya Moetakef,[†] Karen Gaskell,[†] Craig M. Brown,^{‡,§} Graham King,^{||} and Efrain E. Rodriguez^{*,†}

[†]Department of Chemistry & Biochemistry, University of Maryland, College Park, Maryland 20742, United States

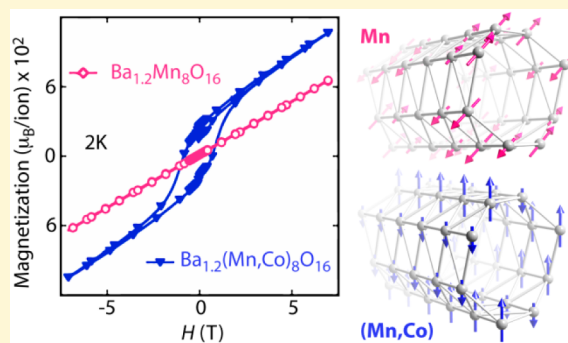
[‡]NIST Center for Neutron Research, National Institute of Standards and Technology, Gaithersburg, Maryland 20899, United States

[§]Department of Chemical and Biomolecular Engineering, University of Delaware, Newark, Delaware 19716, United States

^{||}Lujan Neutron Scattering Center, Los Alamos National Laboratory, Los Alamos, New Mexico 87545, United States

S Supporting Information

ABSTRACT: Magnetic insulators are functional materials with potential applications in spintronics and multiferroics. The hollandites $\text{A}_x\text{M}_8\text{O}_{16}$, which contain mixed-valent transition metals, have demonstrated ferromagnetism combined with insulating behavior and provide a new platform for exploring the effects of magnetic frustration due to their “folded” triangular lattice. We have tuned the hollandite $\text{Ba}_x\text{Mn}_8\text{O}_{16}$ from a complex antiferromagnet with Néel temperature (T_N) = 25 K to a ferrimagnet with Curie temperature (T_C) = 180 K via partial cobalt substitution for manganese. Both $\text{Ba}_x\text{Mn}_8\text{O}_{16}$ and $\text{Ba}_x\text{Co}_y\text{Mn}_{8-y}\text{O}_{16}$ were prepared by salt flux methods, and combined neutron and X-ray diffraction confirm a distorted hollandite-type structure for both oxides. X-ray photoelectron spectroscopy reveals that the Co^{2+} substitution drives the average Mn oxidation state from 3.7+ to nearly 4.0+, thereby changing its d-electron count. Magnetization and resistivity measurements show that the cobalt-doped hollandite is a ferrimagnetic insulator, with a high T_C of 180 K. On the basis of neutron diffraction measurements, we provide the first solution of the magnetic structure of $\text{Ba}_x\text{Mn}_8\text{O}_{16}$, which consists of a complex antiferromagnet with a large magnetic unit cell. Upon substituting cobalt for manganese, the magnetic structure changes dramatically, destroying the previously large magnetic unit cell and promoting ferromagnetic alignment along the hollandite tunnel direction. The observed hysteresis at base temperature for $\text{Ba}_x\text{Co}_y\text{Mn}_{8-y}\text{O}_{16}$ is explained as arising from uncompensated spins aligned along the (200) crystallographic planes.



■ INTRODUCTION

Transition metal oxides with triangular magnetic lattices can lead to new and interesting phenomena on account of their inherently frustrated geometry. In two-dimensional (2D) systems such as A_xMO_2 (A = alkali or alkaline earth, M = transition metal), the triangular lattice can exhibit a rich magnetic-structural phase diagram or exotic states such as spin liquids.^{1–8} In the highly frustrated 2D Kagomé lattice of $\text{A}_x\text{Cu}_{4-x}(\text{OH})_6\text{Cl}_2$, the frustration can be lifted by chemical disorder leading to a ferrimagnetic ground state instead.^{9,10} Less explored are materials in which the triangular lattice is folded in three-dimensional space, leading to new topologies for studying magnetism. Such a folded triangular lattice can be realized in a group of metal oxides with the so-called hollandite structure type (Figure 1a). Here, we study a manganese-based folded triangular lattice and the dramatic changes that occur in its magnetic properties upon cobalt(II) substitution.

Suib et al. coined the term octahedral molecular sieves (OMS) for frameworks featuring MnO_6 octahedra arranged into one-dimensional (1D) tunnels.¹¹ The hollandite OMS features MnO_6 octahedra that share edges and corners to form a 2×2 square tunnel (Figure 1a). Each wall of the 2×2 tunnel

consists of edge-sharing MnO_6 octahedra, so that a triangular ladder connects the Mn centers (Figure 1b). In comparison, the $\alpha\text{-NaMnO}_2$ structure contains a 2D infinite triangular lattice (Figure 1c). Since each wall of the hollandite $\text{Ba}_x\text{Mn}_8\text{O}_{16}$ connects to the others, the overall topology of the Mn centers can be thought of as the triangular lattice folded into a 1D tube (Figure 1d).

The tunability of the cations in the hollandite structure type makes these oxides highly functional for various applications such as molecular sieves,^{12,13} catalysts,^{14,15} and cathode materials in batteries.^{16–18} Indeed, studies of hollandites have already led to promising physical properties such as insulating ferromagnetism in $\text{K}_2\text{Cr}_8\text{O}_{16}$ and metal-to-insulator transitions (T_{MIT}) with antiferromagnetism in $\text{K}_2\text{V}_8\text{O}_{16}$.^{1,19–23} The transition metal sites in hollandite structures can accommodate valencies from 2+ to 5+,^{20,24–26} and mixed valency is a common phenomenon in OMS materials. Just as mixed-valence manganates with the perovskite structure led to interesting

Received: October 15, 2014

Revised: December 3, 2014

Published: December 19, 2014

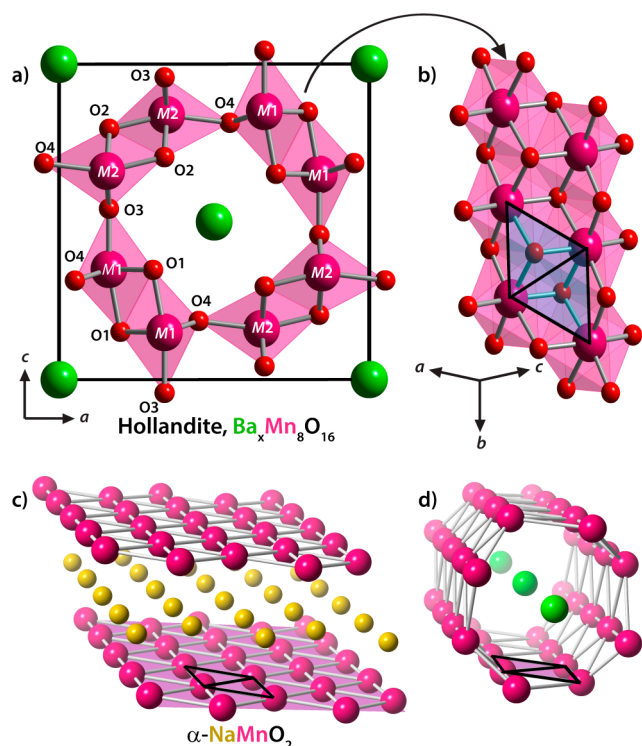


Figure 1. (a) Hollandite structure viewed down the *b* axis. (b) Tunnel wall of hollandite showing a triangular ladder. (c) 2D triangular lattices in $\alpha\text{-NaMnO}_2$ and (d) the triangular lattice tube in hollandite. Oxygen atoms are not shown for clarity in c and d.

phenomena such as charge, spin, and orbital ordering.^{27–29} mixed $\text{Mn}^{3+}/\text{Mn}^{4+}$ cations in hollandites could also lead to similar phenomena. Transition metal site doping in the hollandites has already been undertaken by various researchers to tune the chemical properties.^{30–35} Determining the location(s) of dopant atoms, as well as any potential charge ordering, is key to understanding new physics in the hollandites as well.

The propensity of OMS materials to develop crystallographic defects, such as twinning and/or intergrowth of more than one OMS phase, make it difficult to grow crystals or prepare highly crystalline powders.^{36–38} Recently, Talanov et al. and Moetakef et al. have demonstrated high quality single crystal growth of hollandite oxides through flux methods.^{39,40} Therefore, we have sought to prepare highly crystalline and phase-pure Mn-based hollandites by employing salt flux methods in order to fully explore the relationship between crystal structure and magnetic properties.

We report the nuclear and magnetic structures of $\text{Ba}_x\text{Mn}_8\text{O}_{16}$ (BMO) and a cobalt-doped analogue, $\text{Ba}_x\text{Co}_y\text{Mn}_{1-y}\text{O}_2$ (BCMO). A combination of X-ray and neutron powder diffraction, X-ray photoelectron spectroscopy, magnetometry, and electronic transport studies were utilized to investigate the morphology, thermal stability, composition, magnetic, and electrical properties. Our results suggest that Mn-based hollandites are good candidates for exploring the possibility of magnetic semiconductors, an important set of materials for spintronic applications.

EXPERIMENTAL SECTION

Sample Preparation. Samples were synthesized through the salt flux method described by Ishiwata et al. to produce the polycrystalline

hollandite, $\text{Ba}_{1.2}\text{Mn}_8\text{O}_{16}$.⁴¹ Starting reagents included KCl (99.2%, J.T. Baker), Mn_2O_3 (99%, Sigma-Aldrich), Co_3O_4 (74%-gravimetric Co, Sigma-Aldrich), and $\text{Ba}(\text{NO}_3)_2$ (99.999%, Sigma-Aldrich).⁴² Reagents were used without further purification.

A powder mixture with a molar ratio of 1.2:4:12 of $\text{Ba}(\text{NO}_3)_2$, Mn_2O_3 , and KCl was ground with an agate mortar and pestle to obtain a target stoichiometry of $\text{Ba}_{1.2}\text{Mn}_8\text{O}_{16}$ (BMO). For the cobalt-doped sample, a stoichiometric mixture of the metals was mixed with the KCl flux in a 1:12 ratio to target a stoichiometry of $\text{Ba}_{1.2}\text{CoMn}_7\text{O}_{16}$ (BCMO). Both materials were then heated in covered alumina crucibles under ambient atmosphere. Heating was maintained at a rate of 100 K/h up to 1123 K, soaked for 72 h, then cooled to room temperature at 100 K/h. The obtained samples were washed in DI water to dissolve KCl and dried at 373 K for 1 h. Small impurities of BaCO_3 were removed by stirring samples in 1 M HCl for 30 min, followed by washing with DI H_2O until pH returned to neutral.

For inductively coupled plasma mass spectrometry (ICP-MS) measurements, ~ 10 mg of sample was stirred in 5 mL of concentrated HCl until completely dissolved then diluted appropriately for analysis. For resistivity measurements, sample powders were pressed into pellets 1 mm thick and 13 mm in diameter. Pellets were sintered at 1173 K for 24 h.

Diffraction, Magnetization, and Spectroscopy. Room temperature powder X-ray diffraction (XRD) data were collected on a Bruker D8 X-ray diffractometer with Cu $K\alpha$ radiation, $\lambda = 1.5418$ Å (step size = 0.013° , with 2θ ranging from 8° – 140°). Time-of-flight (TOF) neutron powder diffraction (NPD) data were collected on the high intensity powder diffractometer (HIPD) beamline at the Lujan Neutron Scattering Center at Los Alamos Neutron Science Center. Low temperature constant wavelength (CW) neutron diffraction data were collected on the BT-1 high resolution powder neutron diffractometer at the NIST Center for Neutron Research. Cu(311) and Ge(311) monochromators produced neutron beams of $\lambda = 1.5403$ Å and $\lambda = 2.078$ Å, respectively. Scans were taken at 5, 10, and 50 K for BMO, and at 10, 40, 80, 120, 160, 180, 250, and 300 K for BCMO.

Magnetic susceptibility measurements were carried out using a magnetic property measurement system (Quantum Design MPMS). Both field-cooled (FC) and zero-field-cooled (ZFC) magnetic susceptibility measurements were taken from 2 K–300 K in direct current mode with an applied magnetic field of 0.01 T (100 Oe). Hysteresis measurements were carried out at 2 K in magnetic fields between ± 7 T.

A Quantum Design physical property measurement system (PPMS) was used for temperature dependent resistivity measurements using a four-probe or Van der Pauw geometry.^{43,44} Sintered pellets were mounted onto a PPMS puck with electrical continuity established by using silver paste to connect gold wires from the pellet to the sample mount.

X-ray photoelectron spectroscopy (XPS) measurements were taken in a high sensitivity Kratos AXIS 165 X-ray photoelectron spectrometer operating in hybrid mode to analyze the composition and average transition metal oxidation state at the surface. For the Mn 2p peaks, monochromatic Al $K\alpha$ at 280 W was used as the X-ray energy source, whereas both Mg $K\alpha$ and monochromatic Al $K\alpha$ sources were utilized (at 280 W) in studying the Co 2p peaks in efforts to better resolve peak overlaps. CasaXPS software was used for quantification and peak fitting after application of Shirley backgrounds using relative sensitivity factors from the Kratos vision library. Pressure was at or below 5×10^{-8} Torr during data collection, and charge neutralization was required to minimize surface charging.

RESULTS AND DISCUSSION

Crystal Structure. As-synthesized XRD patterns were taken to measure crystal structure and purity. Rietveld refinement of both BMO and BCMO structures were carried out with the TOPAS 4.2 software.⁴⁵ The patterns of as-synthesized samples showed good fit to the structure reported by Ishiwata et al.,⁴¹ including an impurity peak at $2\theta \sim 24.1$ – 24.5° , which was reported in the literature but remained unidentified. This peak

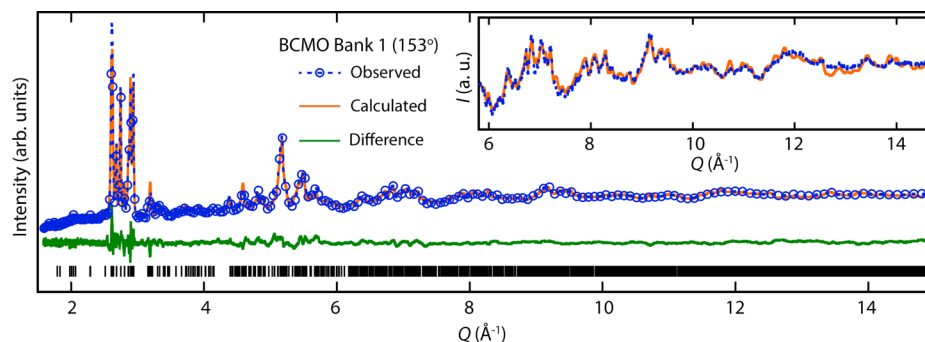


Figure 2. Rietveld refinements with the TOF neutron data (HIPD, Los Alamos) for the structure of BCMO. The highest resolution is found in the backscattering 153° bank, which also has the highest Q -range. The black tick marks indicate expected positions of hollandite reflections. The inset allows for better visualization of the structural details and refinement that occur at $Q > 6 \text{ \AA}^{-1}$. The BCMO fit to the data measured at the 90° and 40° detector banks and the 153°, 90°, and 40° fits of BMO are available in Supporting Information.

corresponds to the impurity phase BaCO_3 . Stirring the sample in 1 M HCl for 30 min followed by washing until the pH returned to neutral removed most of the BaCO_3 phase without diminishing the crystallinity of the oxides.

The crystal structures of BMO and BCMO at room temperature were solved by simultaneously fitting banks 1, 3, and 5 of the TOF neutron diffraction data measured on HIPD (Figure 2 and Supporting Information). The resulting patterns were fit with a monoclinic cell (space group $I2/m$) with the parameters presented in Table 1.

The refined occupancy of the Ba site is 0.28(2) in BMO and 0.27(2) in BCMO, slightly less than the targeted stoichiometry (0.3 per site). This discrepancy can be accounted for in the BaCO_3 impurities removed by HCl washing, which may have also leached a small amount of Ba cations from the hollandite tunnels. The large values for the Ba thermal displacement parameters are likely a result of the loose coordination environment of the Ba cation within the framework, allowing increased tunnel cation mobility. Previous studies of hollandite frameworks have seen incommensurate modulations of the tunnel cation, visible in electron microscopy images as sharp satellite peaks or diffuse intensity normal to the tunnel direction.^{26,46,47}

Composition analysis via Rietveld refinement of neutron data provides a first approximation of whether any cobalt successfully incorporated into the Mn-hollandite. The refined Co occupancy in BCMO is 0.40(8) per unit cell, in contrast to the expected value of 1 per unit cell. However, as the overall Co concentration is small, the error relative to the total amount of Co is large. Although the neutron scattering lengths of Co and Mn have fairly good contrast (2.49 fm in Co vs -3.73 fm in Mn), the absolute values of the scattering lengths are smaller than those of either Ba (5.07 fm) or O (5.803 fm).⁴⁸ Thus, small changes in composition between Mn and Co are expected to only affect small changes in the observed diffraction pattern. The refined composition from neutron data therefore are useful in confirming the presence of Co, but other elemental analyses are capable of achieving greater compositional precision between Mn and Co. We present such methods in the Elemental Analysis section.

We can, however, further evaluate the metal-oxide bond distances determined from diffraction data to infer the amount of Mn^{3+} and Co^{2+} present in BMO and BCMO, respectively. The target stoichiometry of $\text{Ba}_{1.2}\text{Mn}_8\text{O}_{16}$ would lead to an average oxidation state of 3.7+ per manganese cation. Introduction of Co^{2+} into the framework structure should

Table 1. Room Temperature Lattice and Structural Parameters from TOF Neutron Diffraction Refinement

sample		$\text{Ba}_{1.14}\text{Mn}_8\text{O}_{16}$ (BMO)	$\text{Ba}_{1.10}\text{Co}_y\text{Mn}_{8-y}\text{O}_{16}$ (BCMO)
no. of reflections		2545	2560
no. of parameters ^a		29	31
Rwp (%)		7.031	5.109
space group		$I2/m$	$I2/m$
<i>a</i> (Å)		9.683(2)	9.6468(8)
<i>b</i> (Å)		2.8531(5)	2.8589(2)
<i>c</i> (Å)		9.916(2)	9.9954 (8)
β (deg)		88.907(3)	88.654(3)
volume (Å ³)		273.9557(3)	275.6637(1)
calcd density (g/cm ³)		5.161(2)	5.11(8)
4g Ba	<i>y</i>	0.34(2)	0.47(6)
	Occ	0.28(2)	0.27(2)
	<i>B</i> (Å ²)	8(1)	9(2)
4i M1	<i>x</i>	0.170(4)	0.1663(5)
	<i>z</i>	0.353(3)	0.3517(5)
	Occ ^b	1	0.94(1)
	<i>B</i> (Å ²) ^c	0.56(6)	0.32(4)
4i M2	<i>x</i>	0.338(1)	0.3442(5)
	<i>z</i>	0.843(1)	0.8410(6)
	Occ ^b	1	0.961(9)
4i O1	<i>x</i>	0.1936(7)	0.1910(4)
	<i>z</i>	0.165(3)	0.1618(5)
	<i>B</i> (Å ²) ^c	0.221(9)	0.034(6)
4i O2	<i>x</i>	0.1408(8)	0.1401(4)
	<i>z</i>	0.7998(6)	0.7924(4)
4i O3	<i>x</i>	0.1822(9)	0.1839(5)
	<i>z</i>	0.5374(7)	0.5437(5)
4i O4	<i>x</i>	0.5445(7)	0.5500(4)
	<i>z</i>	0.8515(7)	0.8507(5)

^aRefined parameters include 5-order polynomial background, lattice parameters (4), scale (2), zero error (2), atomic positions (13), Ba occupancy (3), thermal displacement parameters (3), and preferred orientation along (1 1 2) and (3 0 3) planes (2). ^bCo occupancy is $1 - x$, where x is the occupancy listed for M1 and M2. ^cAtomic displacement parameters were constrained to be equivalent for M1 and M2, and also for O1–O4.

cause the manganese to oxidize in order to maintain charge balance, with an expected oxidation state per manganese cation of 3.94+ for the target stoichiometry of $\text{Ba}_{1.2}\text{CoMn}_7\text{O}_{16}$. From a bond valence perspective, the lower valent cations are larger

than Mn^{4+} and should thus lead to larger $M\text{—O}$ bond distances.

To assess the effects of Co-substitution on the crystal structure, we must first analyze the metal–oxide bond distances in BMO. As observed in a sample of pyrolusite MnO_2 ,⁴⁹ Mn^{4+} has an average Mn—O bond length of ~ 1.89 Å, whereas Mn^{3+} has an average Mn—O bond length of 2.04 Å.⁵⁰ The average $M\text{—O}$ bond lengths obtained from room temperature refinements of BMO are 1.893 and 1.956 Å for the $M1$ and $M2$ sites, respectively (Table 2). These bond lengths suggest

Table 2. Select Interatomic Distances (Å) and Angles (deg) in BMO at 300 K

bond length (Å)		bond angle (deg)	
$M1\text{—O}3$	1.84 (1)	$M1\text{—O}4\text{—}M1$	98.950
$M1\text{—O}1$	1.948(9) x2	$M1\text{—O}1\text{—}M1$	99.144
	1.87(1)		94.205
$M1\text{—O}4$	1.88(2) x2	$M2\text{—O}3\text{—}M2$	100.082
$M2\text{—O}2$	2.02(3) x2	$M2\text{—O}2\text{—}M2$	93.881
	1.97(2)		89.859
$M2\text{—O}3$	1.86(2) x2	$M1\text{—O}3\text{—}M2$	128.751
$M2\text{—O}4$	2.01(3)	$M1\text{—O}4\text{—}M2$	130.502

that Mn^{4+} preferentially occupies the $M1$ site, while both Mn^{3+} and Mn^{4+} cations occupy the $M2$ site in an approximately 1:1 ratio. These bond distance values imply an average Mn oxidation state of 3.75+ in BMO, slightly higher than the target of 3.7+. We further quantify these values by using the bond valence method of Brown, Brese, and O’Keeffe^{51–53} and use the empirical bond valence parameter for Mn^{4+} . The bond valence calculations lead to the $M1$ site having a valence of 4.12 and the $M2$ site 3.53.

In BCMO, the average bond lengths are 1.908 and 1.942 Å for the $M1$ and $M2$ positions, respectively (Table 3). In a high-

Table 3. Select Interatomic Distances (Å) and Angles (deg) in BCMO at 300 K

bond length (Å)		bond angle (deg)	
$M1\text{—O}3$	1.93(1)	$M1\text{—O}4\text{—}M1$	103.751
$M1\text{—O}1$	1.987(8) x2	$M1\text{—O}1\text{—}M1$	97.915
	1.908(7)		92.028
$M1\text{—O}4$	1.817(7) x2	$M2\text{—O}3\text{—}M2$	101.044
$M2\text{—O}2$	1.958(8) x2	$M2\text{—O}2\text{—}M2$	93.775
	2.04(1)		95.875
$M2\text{—O}3$	1.852(9) x2	$M1\text{—O}3\text{—}M2$	127.132
$M2\text{—O}4$	1.99(1)	$M1\text{—O}4\text{—}M2$	128.088

spin octahedral configuration, Co^{2+} should have a bond length of 2.14 Å.⁵⁰ These values suggest that Mn^{4+} still favors the $M1$ site and that Co^{2+} mixes with Mn^{4+} at the $M2$ position in a nearly 1:3 ratio, assuming no Mn^{3+} is found in BCMO. The same bond valence treatment of the bond distances leads to an $M1$ valence of 4.02 and an $M2$ valence of 3.67. From these calculations, we can further conclude that the charge difference between M sites is diminished in BCMO relative to BMO, as would be expected from the oxidation of Mn upon Co^{2+} substitution. Since these results are obtained from the average structure, we cannot be certain of the location of Co^{2+} based solely on the arguments of average bond length. Thus, further investigations into the local structure from total scattering

studies are underway to determine possible local ordering in BCMO.

The Mn^{3+} cation, which seems to favor the $M2$ atomic position (Figure 1a) in BMO, could potentially undergo a Jahn–Teller (JT)-distortion and therefore elongate in the direction parallel to the a -axis. An evaluation of the bond distances in BMO (Table 2) shows that $M2\text{—O}2$ and $M2\text{—O}4$ are both over 2.0 Å and longer than the other distances. However, this elongation does not correspond to the expected JT-elongation along one axis but instead indicates a trigonal distortion of the octahedra, with one trigonal face further from the metal center than the other. In contrast, the equivalent $M2\text{—O}$ bond distances in BCMO are shortened, which is further evidence that the JT-active Mn^{3+} cation is no longer present in BCMO due to Co^{2+} substitution. Future TOF neutron experiments at temperatures below the magnetic ordering transitions will be helpful to search for possible orbital ordering from JT-distortions.

Elemental Analysis. Before presenting the magnetic properties of BMO and BCMO, we present the elemental analysis undertaken in order to understand the effects of Co-substitution on structure and composition. To this end, we utilized XPS measurements to determine metal oxidation states by studying the 2p and 3s X-ray core level photoelectron spectra and ICP-MS to verify the elemental composition of the samples.

Qualitatively, the asymmetry present in the Mn 2p_{3/2} peak of BMO and BCMO (Figure 3a) matches that reported for mixed-valent Mn by Millitello et al. in LiMn_2O_4 ,⁵⁴ which is consistent with expected mixed valency in hollandites. Unfortunately, the splitting of the Mn 2p peaks is not helpful in assigning definitive oxidation states since literature values for the splitting of Mn^{4+} , $\text{Mn}^{3.5+}$, and Mn^{3+} are 11.7, 11.7, and 11.6 eV, respectively.^{54–56} Furthermore, overlap of the Ba 4d_{5/2} peak

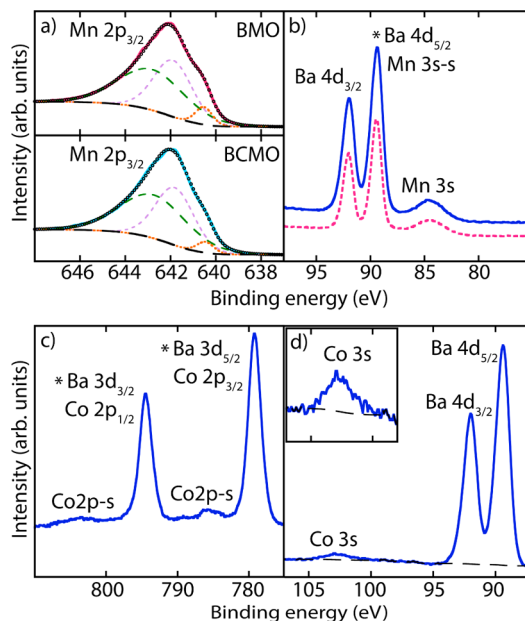


Figure 3. XPS spectra of M 2p and M 3s peaks in BMO (dotted pink) and BCMO (solid blue). $M = \text{Mn}$ in panels a and b, and $M = \text{Co}$ in c and d. $\text{Mn } 2p_{1/2}$ was not shown in panel a to better emphasize the subtle difference in fit of the higher resolution $\text{Mn } 2p_{3/2}$ peak. Asterisks indicate M peaks overlapping with Ba peaks. Dashed black lines show the background used for composition quantification.

with the higher binding energy Mn 3s multiplet (Figure 3b) complicated the analysis since the oxidation state of Mn is most reliably determined via splitting between the two Mn 3s multiplets.⁵⁷

To extract more information about the Mn state from the XPS data, we performed a careful comparison of the Mn 2p_{3/2} peak shape in BMO to that in BCMO. The peak shape for Mn 2p_{3/2} shows an asymmetric shoulder at lower binding energy (Figure 3a). We fit the Mn 2p_{3/2} transition with three peaks constrained to occur at the same binding energies and with the same full width at half maximum between the BMO and BCMO spectra (see data in Table 1 of Supporting Information). A change in the intensity of the lowest binding energy peak is observed, increasing from BCMO to BMO. Previously reported XPS measurements of binary Mn oxides show that the Mn 2p_{3/2} peak occurred at a slightly lower binding energy (−0.6 eV) in Mn₂O₃ than in MnO₂.^{49,50} Thus, if the intensity of the peak fit at lower binding energy is proportional to the amount of Mn³⁺ in the sample, there is more Mn³⁺ present in BMO, leading to a lower average Mn oxidation state than in BCMO.

In the BCMO sample, the Co 2p peaks overlapped with the Ba 3d peaks. The presence of the Co 2p satellite peaks, however, is characteristic of cobalt atoms in the high spin 2+ oxidation state (Figure 3c).^{58,59} These satellite peaks give good certainty to the assumption that the cobalt cations within the bulk of the material are also divalent since the propensity for higher oxidation states is greatest for cations at the surface.⁶⁰

Quantification to obtain surface stoichiometry was carried out using the Ba 3d and 4d peaks for BMO and BCMO, respectively, as well as the Mn 2p and Co 3s peaks. Composition analyses of all obtained methods are listed in Table 4, with XPS measurements resulting in the surface

Table 4. Composition Analyses of BMO and BCMO^a

	BMO		BCMO		
	Ba	Mn	Ba	Co	Mn
neutron	1.14(6)	8	1.09(9)	0.40(9)	7.60(9)
XRD	1.22(1)	8	1.27(2)		
ICP-MS	1.6(3)	8	1.47(5)	0.91(4)	7.09(4)
XPS	1.5(1)	8.0(4)	1.4(1)	0.79(5)	7.2(5)

^aValues indicate the molar ratios determined by the given method.

stoichiometries of Ba_{1.4}Co_{0.79}Mn_{7.2} and Ba_{1.5}Mn₈. In both samples, we see more Ba than expected based on initial stoichiometry. The discrepancy in Ba might be due to Ba cations moving to the surface during either the HCl wash or while the system is in the high vacuum XPS environment.

Investigating the sample composition via ICP-MS gave stoichiometries of Ba_{1.6}Mn₈O₁₆ for BMO, which suggests an average manganese oxidation state of 3.6+. The composition of BCMO via ICP-MS gave a stoichiometry of Ba_{1.5}Co_{0.9}Mn_{7.1}O₁₆. Assuming Co is 2+ (as seen in the XPS data), this leads to an average manganese oxidation state of 3.83+.

Magnetic Properties. Field-cooled (FC) and zero-field-cooled (ZFC) measurements were taken of both samples with and without acid washing (Figure 4a and b). Preliminary analysis of the magnetic susceptibility of BCMO compared to BMO revealed a dramatic change in the magnetic response of the oxide. FC/ZFC curves of BMO show the susceptibility to be virtually identical above 25 K irrespective of the applied magnetic field, with the magnetic responses diverging at low

temperature. The low-temperature divergence of the FC/ZFC curves in the manganese sample agrees with the observations of Suib and Iton, where they classified manganese oxide hollandite materials as spin-glass systems.⁶¹

An increase in magnetic susceptibility (χ) of BCMO was observed with an onset near 180 K and saturation near 22 K, indicative of long-range ferri- or ferromagnetic ordering. The temperature and the magnitude of FC/ZFC divergence of BCMO at 180 K contrast significantly with those observed in the pure manganese sample. At 2 K, the $\Delta\chi$ is $\sim 1 \times 10^{-3}$ between the FC and ZFC curve for BMO, whereas in BCMO the $\Delta\chi$ at 2 K is ~ 1 , a difference of 3 orders of magnitude.

Fitting the linear high temperature region ($T > 225$ K) of the χ^{-1} plots to the Curie–Weiss equation, $\chi = C/(T - \theta_{CW})$, we were able to obtain the effective paramagnetic moment (μ_{eff}), the Curie constant C , and the Curie–Weiss intercept θ_{CW} for BMO and BCMO. The obtained values are recorded in Table 5. Based on the compositions observed via ICP-MS where the average Mn oxidation state is 3.6+, an effective magnetic moment of 4.28 μ_B is expected for BMO. The calculated μ_{eff} value of 4.34 μ_B for the as-prepared BMO sample agrees relatively well with the expected value.

On the basis of the average Mn oxidation state of 3.83+ in BCMO, the spin-only contribution from the manganese cations to the effective magnetic moment should be 4.05 μ_B . A μ_{eff} of $\sim 4.3 \mu_B$ to 5.2 μ_B is the reported value for Co²⁺ cations in the high-spin configuration, a result of both spin and orbital contributions.^{62,63} Thus, in BCMO we would expect the combination of Mn^{3.83+} and Co²⁺ to result in a μ_{eff} of $\sim 4.14 \mu_B$. The obtained value for μ_{eff} in BCMO is instead 4.64 μ_B , which is significantly higher than expected. Since the transition temperature observed in BCMO is 180 K, the linear region used to fit the Curie–Weiss law ($T > 225$ K) in the measured data may be too close to the transition temperature to allow for accurate determination of magnetic constants. We therefore include the Curie constant from the fits for both BMO and BCMO as this may allow a more straightforward assessment of the consequences of substituting Co²⁺ on the bulk magnetic properties.

The decrease in μ_{eff} observed in both samples upon acid washing supports the conclusion that Ba²⁺ cations are deintercalating from the tunnels during the acid wash process, causing the framework transition metal cations to further oxidize. Although the Néel temperature in BMO is 25 K, the absolute value of θ_{CW} for BMO is fairly large indicating strong antiferromagnetic exchange. Ramirez has defined a frustration index f as the ratio of the Weiss field to the ordering temperature, where $f = |\theta_{CW}|/T_N$.^{64,65} A highly frustrated system is classified as one where $f > 10$. In BMO, $f \approx 17$, and such significant spin frustration within the framework is often seen in triangular lattices of edge-sharing MO₆ octahedra (Figure 1).⁶⁶ In BCMO, $f \approx 3.5$, indicating that the Co²⁺ substitution has effectively relieved the highly frustrated state of the hollandite.

The standardized χ^{-1} plot shown in Figure 4c allows for the direct comparison of BMO and BCMO. The dashed line passing through the origin corresponds to ideal Curie–Weiss behavior and can be used to measure the fit quality in the high temperature paramagnetic regime. The observed negative deviations from the ideal Curie–Weiss line indicate uncompensated antiferromagnetism (ferrimagnetism) present in the sample.⁶⁷ Overall, the magnetization data support a partially saturated ferrimagnetic ground state in BCMO.

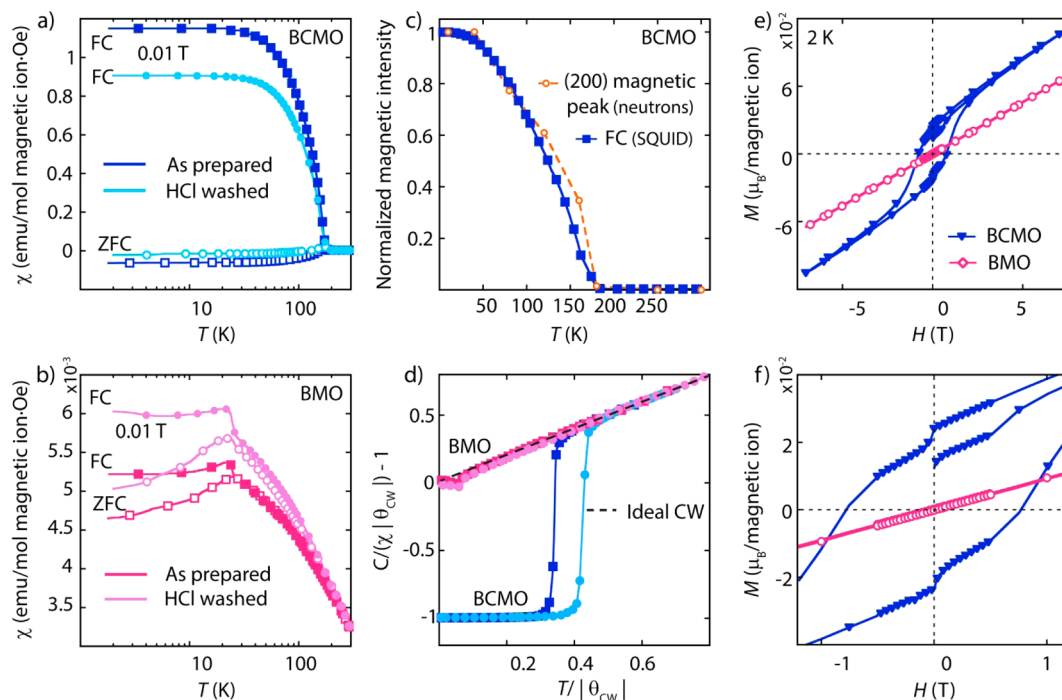


Figure 4. Magnetic susceptibility as a function of temperature for as-prepared and acid-washed samples of BCMO (a) and BMO (b), respectively. (c) Normalized magnetic neutron peaks tracing the field-cooled susceptibility curve of BCMO. (d) Standardized inverse magnetic susceptibility, with the dotted line representing the ideal antiferromagnetic Curie–Weiss fit. Panels e and f show the differences between BMO and BCMO magnetization as a function of applied field.

Table 5. Curie–Weiss Parameters Extracted from High Temperature Paramagnetic Regions of the Inverse Susceptibility Plots Shown in Figure 3

sample	T_N (K)	θ_{CW} (K)	C ($\text{cm}^3 \text{K mol}^{-1}$)	μ_{eff} (μ_B)
BMO (as prepared)	~25	−430	2.34	4.34
BMO (HCl washed)	~25	−335	2.03	4.05
BCMO (as prepared)	~180	−630	2.67	4.64
BCMO (HCl washed)	~180	−499	2.46	4.45

The ferrimagnetic behavior of the BCMO sample contrasts with the Co-doped analogue of a titanium hollandite, $\text{Ba}_{1.3}\text{Co}_{1.3}\text{Ti}_{6.7}\text{O}_{16}$, studied by Shlyk et al., which did not demonstrate any long-range magnetic order down to 2 K. Extrapolation of the high-temperature paramagnetic fit for the titanate hollandite produced a Curie–Weiss constant of $\theta_{CW} = 6.4$ K, indicative of very weak ferromagnetic coupling between the Co ions.⁶⁸ Likewise, the study by Moetakef et al. revealed no long-range magnetic ordering in the hollandite $\text{K}_{1.4}\text{Co}_{0.75}\text{Ti}_{7.25}\text{O}_{16}$.

Magnetization versus magnetic field measurements of BMO and BCMO show that the presence of cobalt within the hollandite structure opens up a hysteresis loop with a coercivity of ~1 T (Figure 4e and f). Magnetic saturation of BCMO was not observed within the field range of the MPMS instrument. To further elucidate the magnetic ordering, neutron powder diffraction patterns were taken of the as-synthesized BCMO sample at (10, 40, 80, 120, 160, 180, 250, and 300) K. One magnetic peak was observed below 180 K, at $2\theta \approx 25^\circ$, which was indexed as the (200) reflection. The observed magnetic peak intensity was normalized and plotted with good agreement to the normalized field-cooled susceptibility of BCMO (Figure 4d). The agreement of these data and successful refinement of the magnetic structure accounting

for the magnetic neutron peaks (discussed later) confirm that the observed magnetization is a property of the bulk sample and is not due to the presence of minute impurities.

Magnetic Structure from Neutrons. As indicated by the magnetization measurements, remarkably different long-range magnetic ordering is observed between BMO and BCMO. To solve the magnetic structures from the base temperature NPD data, we employed the method of representational analysis.

For BMO, we indexed the magnetic Bragg peaks as corresponding to the propagation vector of $\mathbf{k} = (1/4, 1/8, 1/4)$, which corresponds to a large magnetic unit cell with respect to the chemical unit cell ($4a \times 8b \times 4c$). Using the BASIREPS routine in FullProf, we obtained the irreducible representation associated with this \mathbf{k} vector for space group $I2/m$ (Table 6).⁶⁹ The representation indicates that the Mn sites ($M1$ and $M2$) are each split into two orbits (e.g., $M1$ and $M1b$ in Table 6) so that in total there are four independent basis functions. The different orbits are due to each Mn-site having an independent set of basis functions generated by the $2/m$ symmetry of the space group. The refinement was only stable, however, if the two orbits corresponding to the same site were ferromagnetically coupled. This constraint is also due to the paucity of well-defined magnetic reflections in BMO powder sample. From our powder data, the best fit (Figure 5b) led to an antiferromagnetic coupling between $M1$ and $M2$ so that BMO exhibited no net magnetization, as anticipated from the SQUID measurements. The magnetic R -factor from this fit was 46%, while the next model with antiferromagnetic ordering along the b -direction led to a magnetic R -factor of 55%. The next models lead consistently to even higher magnetic R -factors of $\geq 87\%$. Thus, the best fit given the quality of our powder data favors a magnetic moment mostly in the ac -plane.

The complex structure of BMO is depicted in Figure 5c, showing antiferromagnetic moments aligned along the $[1\ 0\ 1]$ -

Table 6. Basis Functions Allowed for the Given Propagation Vector k for Compounds BMO and BCMO^a

	irreducible representation	basis functions
BMO	Γ_1	M1: (1,0,0); (0,1,0); (0,0,1)
		M1 ^b : (1,0,0); (0,1,0); (0,0,1)
		M2: (1,0,0); (0,1,0); (0,0,1)
		M2 ^b : (1,0,0); (0,1,0); (0,0,1)
BCMO	Γ_1	M1,2: (0,1,0)
		M1,2 + $-x,y,-z$: (0,1,0)
	Γ_2	M1,2: (1,0,0); (0,0,1)
		M1,2 + $-x,y,-z$: (1,0,0); (0,0,1)
	Γ_3	M1,2: (1,0,0); (0,0,1)
		M1,2 + $-x,y,-z$: (-1,0,0); (0,0,-1)
	Γ_4	M1,2: (0,1,0)
		M1,2 + $-x,y,-z$: (0,-1,0)

^aThe functions for the different M-cation sites correspond to the magnetic moment directions. In both BMO and BCMO, we conducted the magnetic structure refinements with space group $I-1$.

^bIndicates the second orbit of the M1 and M2 sites. The two orbits are related by the $2/m$ operation.

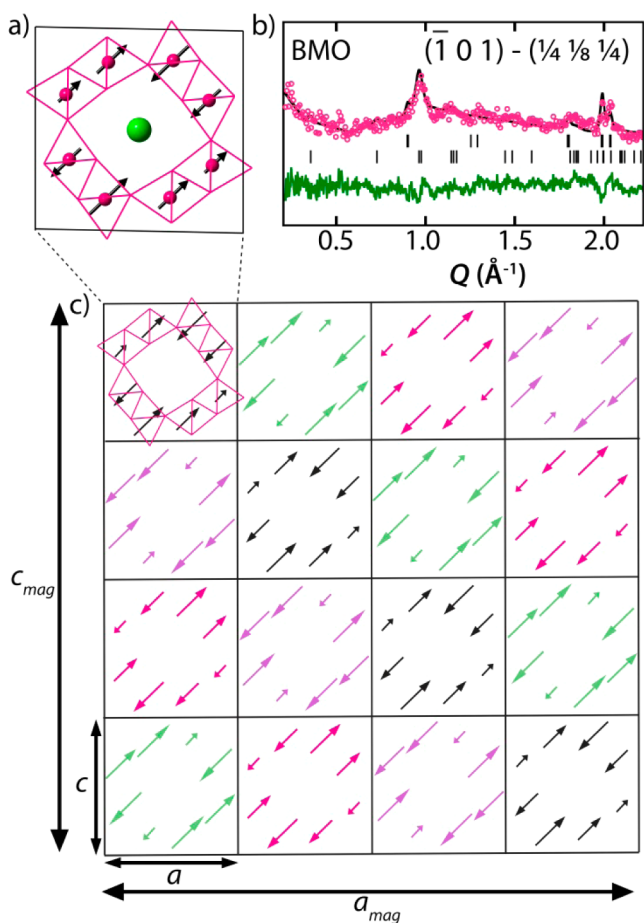


Figure 5. (a) One structural unit cell, with magnetic moments oriented across the cell diagonal in the ac plane. (b) Magnetic fit of constant wavelength data ($\lambda = 2.078$) for BMO, with panel c depicting the resulting complex magnetic structure. Four unique magnetic orderings occur within the structural unit cells, depicted by black, green, magenta, and purple arrows. These cells tile in a pattern such that cells along the $(1\ 0\ 1)$ plane are identical, leading to a long-range modulated magnetic helix.

direction. The direction and size of the moment in the ac -plane is modulated by the propagation vector, indicating that the structure may be that of a complex helical ordering. This is consistent with the helical ordering proposed by Sato et al. for $K_{1.5}\text{Mn}_8\text{O}_{16}$, where they expected the period of the charge ordering (λ_C) to be an integral multiple of the helical magnetic structure. Further, they expected the λ_C to be eight times as large as the unit cell parameter parallel to the tunnel direction (similar to the $8b$ component of our magnetic propagation vector in BMO).^{70,71} The maximum moment size in the ac -plane from fitting the Bragg intensities was $2.3(2)\ \mu_B$, which is lower than the expected $3.2\ \mu_B$ for $\text{Mn}^{3,8+}$ cations. Figure 5a shows a large diffuse background, however, around the most intense satellite peak of $(-1\ 0\ 1)$. Therefore, a large amount of the magnetic moment may be disordered leading to the background instead of contributing to the Bragg reflections.

Remarkably, for BCMO only one magnetic peak was observed at low temperatures, indicating a dramatic change in the magnetic ordering compared to BMO. Moreover, the peak is commensurate with the chemical unit cell and indexes to the (200) peak, which is not symmetry-forbidden in space group $I2/m$ but has no contribution from the nuclear structure. The intensity of the peak decreased as the temperature approached 180 K and completely disappeared by 200 K, consistent with the magnetic transition temperature observed in the susceptibility data (Figure 4d).

Despite resulting in only one major magnetic peak, the magnetic structure of BCMO is not trivial. For the propagation vector of $k = (0\ 0\ 0)$, we obtained the irreducible representations presented in Table 6. Using the Reverse Monte Carlo routine in SARAH, representation Γ_3 gave the lowest residual.⁷² Combinations of Γ_3 with other representations did not result in a lower residual. This representation leads to the moment being only in the ac -plane, as in BMO, but with antiferromagnetic coupling between the Mn sites related by the 2-fold rotational symmetry.

Although several combinations of coefficients for the representations could be chosen to model the magnetic Bragg peaks, three models illustrate our method for finding the most plausible magnetic structure. In Model 1, the representation Γ_3 is used to produce an antiferromagnetic ordering with the moments along the c -direction. We rule out Model 1 since it leads to extra intensity for the $(101)/(-101)$ doublet. Model 2 uses Γ_3 to antialign the moments along the ac -plane in order to remove intensity along the $(101)/(-101)$ reflections but still retain some moment direction along the (200) planes. We disqualify Model 2, however, since it leads to a large intensity for the (002) reflection. Finally, Model 3, which best fit the neutron data, uses Γ_3 but breaks the 2-fold symmetry between the Mn sites. This leads to an antiferromagnetic model, intermediate between Models 1 and 2.

The final antiferromagnetic model in Figure 6 illustrates several points observed in the magnetization data. The source of the uncompensated magnetization at zero-field arises from the moments on one set of (200) planes having a larger component along the c -direction than the antialigned moments. Since the underlying structure is antiferromagnetic, the hysteresis curve never fully saturates even at an applied field of 7 T. Most notably, the moments are ferromagnetically aligned along the tunnel direction in BCMO, whereas in BMO, the moments were antiferromagnetically aligned with the magnetic cell along the tunnel direction being 8 unit cells long.

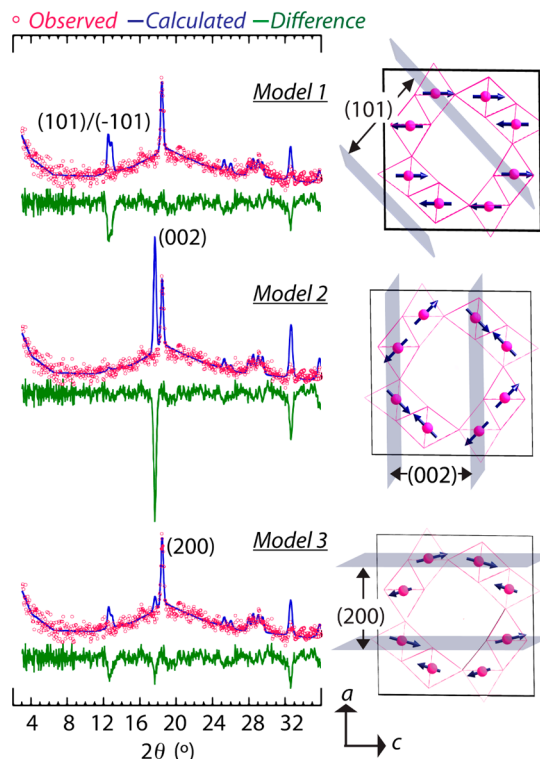


Figure 6. Three different models of the magnetic structure of BCMO and their corresponding fits to the neutron powder patterns. The neutron data were taken at the BT-1 powder diffractometer at NIST with a $\lambda = 1.54 \text{ \AA}$. The best refinement was achieved in Model 3, where the moments are mostly in the (200) plane with some ferrimagnetism arising from uncompensated moments for half of the metal sites.

Electrical Properties. The resistivity of BMO was previously measured by Ishiwata et al., where they observed insulating behavior with room temperature resistivity of $\sim 3 \times 10^2 \text{ } \Omega\cdot\text{cm}$.⁴¹ Figure 7 shows the electrical resistivity measure-

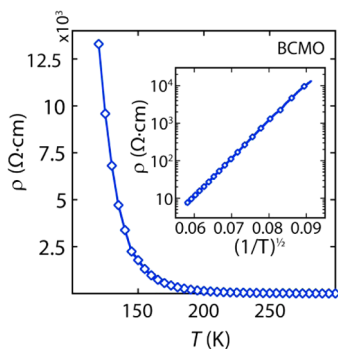


Figure 7. Resistivity of BCMO as a function of temperature. The inset shows linear fitting of resistance versus $T^{-1/2}$ consistent with either one-dimensional Mott or Efros–Shklovskii variable range hopping.

ments of pressed pellets of BCMO. An increase in resistivity upon decreasing temperature indicates insulating behavior, which is likely dominated by grain boundary effects.⁴⁴ Resistivity values obtained from pressed pellets can be 2–3 orders of magnitude greater than their single crystal counterparts, and as such, quantitative conclusions may be inaccurate.⁷³ This is especially true in materials which could exhibit anisotropic conduction as the resistivity values obtained for a

pressed pellet are averaged over all crystallographic orientations.

The fit of the linear plot in the inset is consistent with variable range hopping (VRH) as the mechanism of charge mobility in the cobalt-doped sample. Efros–Shklovskii (ES) variable range hopping is expressed through the following formula:

$$\rho(T) = \rho(T_0) \exp((T_0/T)^{1/2}) \quad (1)$$

where T_0 is a characteristic temperature. In Mott VRH, the exponent in eq 1 changes to $1/(1+d)$, where d is the dimensionality of the electron hopping within the system. Very little difference is seen between the 1D, 2D, and 3D linear fits of Mott VRH, with the best fit observed for one dimension. The fit to eq 1 is consistent with the observations of 1D Mott VRH made by Ishiwata et al. in the pure manganese $\text{Ba}_{1.2}\text{Mn}_8\text{O}_{16}$ system.⁴¹ However, due to the doped nature of BCMO, the ES mechanism seems more likely as Coulomb interactions of dopant atoms would create a gap in the density of states near the Fermi level at low temperatures.

Magnetic Exchange Interactions in Hollandites.

Predicting the magnetic ordering models in hollandites requires an understanding of the various exchange interactions between the cation centers. The recent first-principles and modeling work by Seriani et al. has examined the rich magnetic phase diagrams in hollandite-type $\alpha\text{-MnO}_2$,^{74,75} providing a framework from which to understand BMO and BCMO. Depending on whether the spin Hamiltonian is defined as purely Ising or Heisenberg in nature, Seriani et al. have found various helical, ferromagnetic, collinear antiferromagnetic, and glassy spin states in the phase diagram of $\alpha\text{-MnO}_2$.^{74,75} The theoretical framework by Seriani et al. therefore points to the possible magnetic functional behavior of Mn-based hollandites that we are just starting to explore experimentally.

Given the localized and insulating electronic behavior in BMO and BCMO, we expect superexchange interactions between the cations to dominate the magnetic behavior. We use the notation and models of $\alpha\text{-MnO}_2$ by Seriani et al. to describe the possible exchange parameters, J_i ,^{74,75} found in our oxides. Figure 8 shows the three nearest neighbor exchange interactions arising from the triangular topology of the Mn-sublattice. Along the tunnel direction is J_1 , while J_2 and J_3 act around the tunnel walls. Crystallographic data shows that J_1

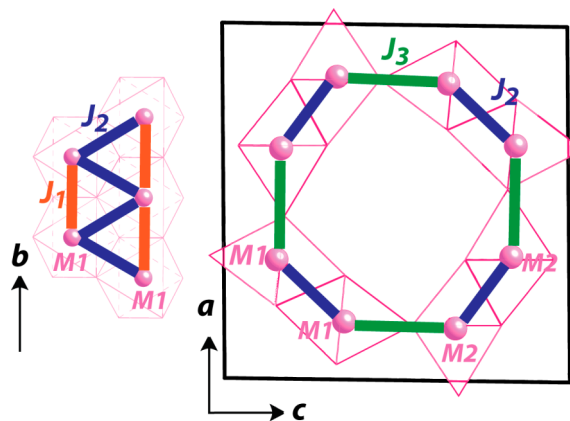


Figure 8. Schematic of the three exchange parameters, J_i , to model the magnetic behavior in BMO and BCMO. This J_1 – J_2 – J_3 model is derived from the theoretical work of Seriani et al.^{74,75}

occurs for the shortest $M-M$ distance in BMO and through the smallest $M-O-M$ bond angle (89.9° to 99.1°). The $M-M$ distances and $M-O-M$ bond angles are subsequently larger for J_2 and J_3 . Notably, J_3 couples the two different M1 and M2 sites in BMO, whereas J_1 and J_2 link the same site within the octahedral dimer chain.

According to the Goodenough–Kanamori rules,^{28,76,77} the superexchange mechanism favors strong, antiferromagnetic interactions when the $M-O-M$ bond angle is 180° . The covalent nature of the orbital overlap between the d-orbitals directed toward the same oxygen p-orbital leads to antiferromagnetic coupling between nearest neighbor cations. When the $M-O-M$ bond angle is 90° , the same d-orbitals in the metal cations interact with orthogonal oxygen p-orbitals, which causes the interaction to be dominated by a Coulombic term that favors a weak, ferromagnetic coupling. In the hollandites presented here, the $M-O-M$ bond angles range from $\sim 90^\circ$ to 130° , which makes assignment of the exchange constants difficult. Unlike in the perovskite manganites, the O^{2-} anions in hollandites coordinate to three metal centers, where half of the oxygen sites are in a trigonal pyramidal geometry, while the other half in trigonal planar. Crespo and Seriani therefore formulated the intermediating orbitals controlling superexchange as the sp^3 hybrid, sp^2 hybrid, and p_z -orbitals.⁷⁸ The sp^3 hybrid is thought to favor ferromagnetic interactions, and the sp^2 and p_z -orbitals can change from antiferromagnetic to ferromagnetic depending on the contribution from the p_z -orbital in hybridizing with the Mn d-orbitals.

The subsequent models from applying these exchange constants led Seriani et al. to find four collinear models: three antiferromagnetic and one ferromagnetic,^{74,75} and they constructed a phase diagram plotting J_2/J_1 vs J_3/J_1 . In an Ising system when J_2 and J_3 are smaller than J_1 , a spin glass state is formed. In a Heisenberg system when J_2 and J_3 are smaller than J_1 , as is likely for Mn^{4+} , various helical states are found. Unfortunately, none of the collinear antiferromagnetic models proposed by Seriani et al. fit the neutron data for BCMO. Nevertheless, our proposed model (Figure 6) is closely related to their antiferromagnetic models with moments along the c -direction as well. We believe that the discrepancy may arise from the chemical composition and structural details between BCMO and α - MnO_2 being substantially different. However, the J_1 – J_2 – J_3 model does explain how Co-substitution could change the ordering in BMO. For BMO, the size of J_2 and J_3 would have to be sufficiently small with respect to J_1 to lead to a helical ordering. The addition of the Co^{2+} cation could tune the system from Heisenberg to Ising-like due to its large single-ion magnetic anisotropy,⁶⁰ thereby unraveling the helical ordering. In addition, the Co^{2+} cations could increase the strength of either J_2 or J_3 sufficiently to promote a collinear state. The structural details from the neutron data do not reveal any obvious changes between BMO and BCMO, so the tuning of the exchange parameters implies an electronic effect rather than a structural one.

CONCLUSIONS

The combination of ferromagnetism with insulating properties is rare as ferromagnetic coupling often involves itinerant electrons. Insulating materials, however, typically feature localized electrons. Several strategies have been pursued to find magnetic insulators in transition metal oxides,^{79–81} especially in perovskite materials.^{82,83} The hollandites represent a new avenue for ferromagnetic insulators, with the study by

Hasegawa et al. representing the first observation of this phenomenon for hollandites. The high-pressure phase $K_2Cr_8O_{16}$ displayed ferromagnetic half-metal behavior with $T_C = 180$ K and T_{MIT} at 95 K.¹⁹ Computational studies on the $K_2Cr_8O_{16}$ material suggest two conflicting models to account for the ferromagnetic insulating properties: Mahadevan et al. suggest the properties arise from charge-ordering within the framework, induced by electrons from the donor tunnel cations,⁸⁴ whereas Toriyama et al. attribute the metal–insulator transition (T_{MIT}) to a Peierls instability in the quasi-one-dimensional structure along the CrO_6 zigzag chains.⁸⁵ Sugiyama et al. lend credence to Toriyama's proposed mechanism in their reports of muon-spin rotation and relaxation data that suggest the absence of charge ordering in $K_2Cr_8O_{16}$ at T_{MIT} .⁸⁶ Deintercalation of potassium from the $K_2Cr_8O_{16}$ framework increased the T_C of the material to 250 K, but no report has been given on resulting electronic properties.⁸⁷ Similarly, the high-pressure phase $Rb_2Cr_8O_{16}$ was reported to be ferromagnetic with a $T_C = 295$ K and semiconducting behavior below ~ 290 K, though this material has only been minimally investigated.^{86,88}

Mn-based hollandites represent a route toward magnetic insulators without the need for high-pressure synthesis. We compare our results in this article with those of other magnetic hollandites in Table 7. In $K_{1.5}Mn_8O_{16}$, Sato et al. reported an

Table 7. Comparison of Magnetic Properties in Reported Ferromagnetic Insulating Hollandites

composition	T_C (K)	coercivity ($T = x$ K)
$K_2Cr_8O_{16}$ ¹⁹	180	$\ll 0.25$ T (5 K)
$Rb_2Cr_8O_{16}$ ⁸⁸	295	
$K_{1.5}(H_3O)_xMn_8O_{16}$ ⁷¹	52	0.4 T (30 K)
BCMO	180	1 T (2 K)

increase of susceptibility (χ) upon cooling from 52 to 20 K, although the susceptibility did not feature any saturation; rather, it peaked at ~ 23 K, then displayed a decrease in susceptibility, characteristic of antiferromagnetic ordering.^{70,71} Magnetic hysteresis measurements of $K_{1.5}Mn_8O_{16}$ at 30 K also failed to saturate, similar to the measurement of BCMO (Figure 4e,f). We believe $K_{1.5}Mn_8O_{16}$ to be closely related to our pure manganese sample, BMO, and that the hysteresis observed by Sato et al. was measured in the small susceptibility hump observed in the transition between paramagnetic and antiferromagnetic behaviors. To the best of our knowledge, no other hollandite materials have been reported with this unusual combination of properties.

Complex helical ordering has been proposed as the magnetic structure of pure manganese-based hollandites $K_{1.5}Mn_8O_{16}$ and $Ba_{1.2}Mn_8O_{16}$.^{41,70,71} We have provided the first magnetic structure refinement of this material from neutron diffraction. The expansion and modulation of the magnetic moments relative to the atomic unit cell support the complex helices that have previously been suggested. The complex helix could represent a way to lift the frustration in the triangular lattice, as evidenced by the high frustration index seen in our magnetization measurements.

By simply substituting enough Mn-sites with Co^{2+} , we have tuned the magnetic ordering from a complex helix to a ferrimagnetic material with a much higher ordering temperature of 180 K. This ferrimagnetic response could now represent another mechanism for relieving the inherently frustrated

lattice. Further total scattering studies are underway to investigate local charge and dopant orderings in both BMO and BCMO.

Our results suggest the possibility of rich electrical and magnetic phase diagrams for OMS materials. The combination of ferrimagnetic and insulating properties suggests that BCMO and future related hollandite materials may have potential use in multifunctional applications such as spintronics. The potential to tune T_C to higher temperatures (as seen in $K_2Cr_8O_{16}$ and $K_2V_8O_{16}$) is especially promising, as future device applications will require functionality near or above room temperature. Furthermore, $K_2Cr_8O_{16}$ and $RbCr_8O_{16}$ require high-pressure preparation,^{88,89} whereas Mn-based hollandites represent a platform for synthesizing magnetic insulators at ambient pressure. A recent study of $BaMn_3Ti_4O_{14.25}$ with the hollandite framework also confirms the possibility of developing these materials for multiferroic applications.⁹⁰ Finally, the microporous nature of hollandite materials further provides interesting possibilities in terms of chemical control of physical applications through soft chemical techniques. With so many tunable variables and possible applications, the family of materials with the hollandite structure type has the potential to significantly affect the fields of materials chemistry and design.

■ ASSOCIATED CONTENT

● Supporting Information

Room temperature time-of-flight neutron structure refinement for BMO. This material is available free of charge via the Internet at <http://pubs.acs.org>.

■ AUTHOR INFORMATION

Corresponding Author

*E-mail: efrain@umd.edu.

Notes

The authors declare no competing financial interest.

■ ACKNOWLEDGMENTS

This work has benefited from the use of the HIPD beamline at the Lujan Center at Los Alamos Neutron Science Center. Los Alamos National Laboratory is operated by Los Alamos National Security LLC under DOE Contract DE-AC52-06NA25396. We also acknowledge the support of the National Institute of Standards and Technology, U.S. Department of Commerce, in providing the neutron research facilities used in this work. We are grateful for the collaboration of Sarah Stoll and Vidumin Dahanayake of the Georgetown University Chemistry Department in obtaining the ICP-MS measurements of our samples. We acknowledge the support of the Maryland NanoCenter, the X-ray Crystallography Center, Surface Analysis Center, and NispLab.

■ REFERENCES

- (1) Isobe, M.; Koishi, S.; Kouno, N.; Yamaura, J.-I.; Yamauchi, T.; Ueda, H.; Gotou, H.; Yagi, T.; Ueda, Y. *J. Phys. Soc. Jpn.* **2006**, *75*, 073801.
- (2) Vecchini, C.; Poienar, M.; Damay, F.; Adamopoulos, O.; Daoud-Aladine, A.; Lappas, A.; Perez-Mato, J. M.; Chapon, L. C.; Martin, C. *Phys. Rev. B* **2010**, *82*, 094404.
- (3) Damay, F.; Poienar, M.; Martin, C.; Maignan, A.; Rodriguez-Carvajal, J.; André, G.; Doumerc, J. *Phys. Rev. B* **2009**, *80*, 094410.

- (4) Li, X.; Ma, X.; Su, D.; Liu, L.; Chisnell, R.; Ong, S. P.; Chen, H.; Toumar, A.; Idrobo, J.; Lei, Y.; Bai, J.; Wang, F.; Lynn, J. W.; Lee, Y. S.; Ceder, G. *Nat. Mater.* **2014**, *13*, 586.
- (5) Giot, M.; Chapon, L. C.; Androulakis, J.; Green, M. A.; Radaelli, P. G.; Lappas, A. *Phys. Rev. Lett.* **2007**, *99*, 247211.
- (6) Stock, C.; Chapon, L.; Adamopoulos, O.; Lappas, A.; Giot, M.; Taylor, J.; Green, M.; Brown, C.; Radaelli, P. *Phys. Rev. Lett.* **2009**, *103*, 077202.
- (7) Kruk, I.; Zajdel, P.; van Beek, W.; Bakaimi, I.; Lappas, A.; Stock, C.; Green, M. A. *J. Am. Chem. Soc.* **2011**, *133*, 13950.
- (8) Abakumov, A. M.; Tsirlin, A. A.; Bakaimi, I.; Van Tendeloo, G.; Lappas, A. *Chem. Mater.* **2014**, *26*, 3306.
- (9) Shores, M. P.; Nytko, E. A.; Bartlett, B. M.; Nocera, D. G. *J. Am. Chem. Soc.* **2005**, *127*, 13462.
- (10) Chu, S.; McQueen, T. M.; Chisnell, R.; Freedman, D. E.; Muller, P.; Lee, Y. S.; Nocera, D. G. *J. Am. Chem. Soc.* **2010**, *132*, 5570.
- (11) Shen, Y.; Zenger, R. P.; Suib, S. L.; McCurdy, L.; Potter, D. I.; O'Young, C.-L. *J. Chem. Soc. Chem. Commun.* **1992**, *17*, 1213.
- (12) Shen, Y. F.; Zenger, R. P.; Deguzman, R. N.; Suib, S. L.; McCurdy, L.; Potter, D. I.; O'Young, C. L. *Science* **1993**, *260*, 511.
- (13) Feng, Q.; Kanoh, H.; Ooi, K. *J. Mater. Chem.* **1999**, *9*, 319.
- (14) Tang, X.; Li, J.; Hao, J. *Catal. Commun.* **2010**, *11*, 871.
- (15) Shen, X.; Ding, Y.; Liu, J.; Laubernds, K.; Zenger, R. P.; Polverejan, M.; Son, Y.-C.; Aindow, M.; Suib, S. L. *Chem. Mater.* **2004**, *16*, 5327.
- (16) Feng, Q.; Kanoh, H.; Ooi, K.; Tani, M.; Nakacho, Y. *J. Electrochem. Soc.* **1994**, *141*, L135.
- (17) Barbato, S.; Gautier, J. L. *Electrochim. Acta* **2001**, *46*, 2767.
- (18) Takeuchi, K. J.; Yau, S. Z.; Menard, M. C.; Marschilok, A. C.; Takeuchi, E. S. *ACS Appl. Mater. Interfaces* **2012**, *4*, 5547.
- (19) Hasegawa, K.; Isobe, M.; Yamauchi, T.; Ueda, H.; Yamaura, J.-I.; Gotou, H.; Yagi, T.; Sato, H.; Ueda, Y. *Phys. Rev. Lett.* **2009**, *103*, 146403.
- (20) Isobe, M.; Koishi, S.; Yamazaki, S.; Yamaura, J.; Gotou, H.; Yagi, T.; Ueda, Y. *J. Phys. Soc. Jpn.* **2009**, *78*, 114713.
- (21) Isobe, M.; Koishi, S.; Ueda, Y. *J. Magn. Magn. Mater.* **2007**, *310*, 888.
- (22) Horiuchi, S.; Shirakawa, T.; Ohta, Y. *Phys. Rev. B* **2008**, *77*, 155120.
- (23) Komarek, A. C.; Isobe, M.; Hemberger, J.; Meier, D.; Lorenz, T.; Trots, D.; Cervellino, A.; Fernández-Díaz, M. T.; Ueda, Y.; Braden, M. *Phys. Rev. Lett.* **2011**, *107*, 027201.
- (24) Kesson, S. E.; White, T. J. *J. Solid State Chem.* **1986**, *63*, 122.
- (25) Ishige, Y.; Sudayama, T.; Wakisaka, Y.; Mizokawa, T.; Wadati, H.; Sawatzky, G. A.; Regier, T. Z.; Isobe, M.; Ueda, Y. *Phys. Rev. B* **2011**, *83*, 125112.
- (26) Carter, M. L.; Withers, R. L. *J. Solid State Chem.* **2005**, *178*, 1903.
- (27) Coey, J. M. D.; Viret, M.; von Molnár, S. *Adv. Phys.* **1999**, *48*, 167.
- (28) Goodenough, J. B. *Phys. Rev.* **1955**, *100*, 564.
- (29) Rodriguez, E. E.; Proffen, T.; Llobet, A.; Rhyne, J. J.; Mitchell, J. F. *Phys. Rev. B* **2005**, *71*, 104430.
- (30) Suib, S. L. *Acc. Chem. Res.* **2008**, *41*, 479.
- (31) Chen, X.; Shen, Y.-F.; Suib, S. L.; O'Young, C. L. *Chem. Mater.* **2002**, *14*, 940.
- (32) King'onde, C. K.; Opembe, N.; Chen, C.; Ngala, K.; Huang, H.; Iyer, A.; Garces, H. F.; Suib, S. L. *Adv. Funct. Mater.* **2010**, *21*, 312.
- (33) Cui, H.-J.; Liu, F.; Tan, W.-F.; Feng, X.-H. *Pedosphere* **2011**, *21*, 730.
- (34) DeGuzman, R. N.; Shen, Y.-F.; Neth, E. J.; Suib, S. L.; O'Young, C.-L.; Levine, S.; Newsam, J. M. *Chem. Mater.* **1994**, *6*, 815.
- (35) Shen, X.; Morey, A. M.; Liu, J.; Ding, Y.; Cai, J.; Durand, J.; Wang, Q.; Wen, W.; Hines, W. A.; Hanson, J. C.; Bai, J.; Frenkel, A. I.; Reiff, W.; Aindow, M.; Suib, S. L. *J. Phys. Chem. C* **2011**, *115*, 21610.
- (36) Post, J. E.; Von Dreele, R. B.; Buseck, P. R. *Acta Crystallogr., Sect. B* **1982**, *38*, 1056.
- (37) Turner, S.; Buseck, P. R. *Science* **1979**, *203*, 456.
- (38) Turner, S.; Buseck, P. R. *Science* **1981**, *212*, 1024.

- (39) Talanov, A.; Phelan, W. A.; Kelly, Z. A.; Siegler, M. A.; McQueen, T. M. *Inorg. Chem.* **2014**, *53*, 4500.
- (40) Moetakef, P.; Larson, A. M.; Hodges, B. C.; Zavalij, P.; Gaskell, K. J.; Piccoli, P. M.; Rodriguez, E. E. *J. Solid State Chem.* **2014**, *220*, 45.
- (41) Ishiwata, S.; Bos, J. W. G.; Huang, Q.; Cava, R. J. *J. Phys.: Condens. Matter* **2006**, *18*, 3745.
- (42) Identification of commercial equipment or products in the text is not intended to imply any recommendation or endorsement by the National Institute of Standards and Technology.
- (43) Van der Pauw, L. J. *Philips Technol. Rev.* **1958**, *20*, 220.
- (44) DeGuzman, R. N.; Awaluddin, A.; Shen, Y.; Tian, Z. R.; Suib, S. L.; Ching, S.; Oyoung, C. *Chem. Mater.* **1995**, 1286.
- (45) Cheary, R. W.; Coelho, A. J. *Appl. Crystallogr.* **1992**, *25*, 109.
- (46) Post, J. E.; Burnham, C. W. *Am. Mineral.* **1986**, *71*, 1178.
- (47) Aubin-Chevaldonnet, V.; Deniard, P.; Evain, M.; Leinekugel-Le-Cocq-Errien, A. Y.; Jobic, S.; Courant, D.; Petricek, V.; Advocat, T. Z. *Krist.* **2007**, *222*, 383.
- (48) Dianoux, A.-J.; Lander, G., Eds. *Neutron Data Booklet*, 2nd ed.; Old City Publishing Group: Philadelphia, PA, 2003.
- (49) Baur, W. H. *Acta Crystallogr., Sect. B* **1976**, *32*, 2200.
- (50) Shannon, R. D. *Acta Crystallogr., Sect. A* **1976**, *32*, 751.
- (51) Brown, I. D.; Altermatt, D. *Acta Crystallogr.* **1985**, 244.
- (52) Brese, N. E.; O'Keeffe, M. *Acta Crystallogr., Sect. B* **1991**, *47*, 192.
- (53) O'Keeffe, M.; Brese, N. E. *J. Am. Chem. Soc.* **1991**, *113*, 3226.
- (54) Militello, M. C.; Gaarenstroom, S. W. *Surf. Sci. Spectra* **2001**, *8*, 207.
- (55) Stranick, M. A. *Surf. Sci. Spectra* **1999**, *6*, 31.
- (56) Stranick, M. A. *Surf. Sci. Spectra* **1999**, *6*, 39.
- (57) Cerrato, J. M.; Hochella, M. F.; Knocke, W. R.; Dietrich, A. M.; Cromer, T. F. *Environ. Sci. Technol.* **2010**, *44*, 5881.
- (58) Petitto, S. C.; Marsh, E. M.; Carson, G. A.; Langell, M. A. *J. Mol. Catal. A: Chem.* **2008**, *281*, 49.
- (59) Hassel, M.; Freund, H.-J. *Surf. Sci. Spectra* **1996**, *4*, 273.
- (60) Oku, M.; Sato, Y. *Appl. Surf. Sci.* **1992**, *55*, 37.
- (61) Suib, S. L.; Iton, L. E. *Chem. Mater.* **1994**, *6*, 429.
- (62) Carlin, R. L. *Magnetochemistry*; Springer-Verlag: Berlin, 1986.
- (63) West, A. R. *Basic Solid State Chemistry*, 2nd ed.; John Wiley & Sons: New York, 1999.
- (64) Ramirez, A. P. *Annu. Rev. Mater. Sci.* **1994**, *24*, 453.
- (65) Greedan, J. E. *J. Mater. Chem.* **2001**, *11*, 37.
- (66) Joy, P. A.; Kumar, P. S. A.; Date, S. K. *J. Phys.: Condens. Matter* **1998**, *10*, 11049.
- (67) Melot, B. C.; Drewes, J. E.; Seshadri, R.; Stoudenmire, E. M.; Ramirez, A. P. *J. Phys.: Condens. Matter* **2009**, *21*, 216007.
- (68) Shlyk, L.; Niewa, R. Z. *Naturforsch., B: J. Chem. Sci.* **2011**, *66*, 1097.
- (69) Rodriguez-Carvajal, J. *Phys. B* **1993**, *192*, 55.
- (70) Sato, H.; Yamaura, J.-I.; Enoki, T.; Yamamoto, N. *J. Alloys Compd.* **1997**, 262–263, 443.
- (71) Sato, H.; Enoki, T.; Yamaura, J.-I.; Yamamoto, N. *Phys. Rev. B* **1999**, *59*, 836.
- (72) Wills, A. S. *Phys. B* **2000**, *680*, 276.
- (73) Coleman, L. B. *Rev. Sci. Instrum.* **1978**, *49*, 58.
- (74) Crespo, Y.; Andreanov, A.; Seriani, N. *Phys. Rev. B* **2013**, *88*, 014202.
- (75) Mandal, S.; Andreanov, A.; Crespo, Y.; Seriani, N. *Condens. Matter* **2014**, 11.
- (76) Goodenough, J. B. *J. Phys. Chem. Solids* **1958**, *6*, 287.
- (77) Kanamori, J. *J. Phys. Chem. Solids* **1959**, *10*, 87.
- (78) Crespo, Y.; Seriani, N. *Phys. Rev. B* **2013**, *88*, 144428.
- (79) Hill, N. A. *J. Phys. Chem. B* **2000**, *104*, 6694.
- (80) Ederer, C.; Spaldin, N. A. *Nat. Mater.* **2004**, *3*, 849.
- (81) Risbud, A. S.; Spaldin, N. A.; Chen, Z. Q.; Stemmer, S.; Seshadri, R. *Phys. Rev. B* **2003**, *68*, 205202.
- (82) Van Aken, B. B.; Palstra, T. T. M.; Filippetti, A.; Spaldin, N. A. *Nat. Mater.* **2004**, *3*, 164.
- (83) Baettig, P.; Spaldin, N. A. *Appl. Phys. Lett.* **2005**, *86*, 012505.
- (84) Mahadevan, P.; Kumar, A.; Choudhury, D.; Sarma, D. D. *Phys. Rev. Lett.* **2010**, *104*, 256401.
- (85) Toriyama, T.; Nakao, A.; Yamaki, Y.; Nakao, H.; Murakami, Y.; Hasegawa, K.; Isobe, M.; Ueda, Y.; Ushakov, A. V.; Khomskii, D. I.; Streltsov, S. V.; Konishi, T.; Ohta, Y. *Phys. Rev. Lett.* **2011**, *107*, 266402.
- (86) Sugiyama, J.; Nozaki, H.; Månsson, M.; Prša, K.; Andreica, D.; Amato, A.; Isobe, M.; Ueda, Y. *Phys. Rev. B* **2012**, *85*, 214407.
- (87) Pirrotta, I.; Fernandez-Sanjulian, J.; Moran, E.; Alario-Franco, M.; Gonzalo, E.; Kuhn, A.; Garcia-Alvarado, F. *Dalton Trans.* **2012**, *41*, 1840.
- (88) Okada, H.; Kinomura, N.; Kume, S.; Koizumi, M. *Mater. Res. Bull.* **1978**, *13*, 1047.
- (89) Sugiyama, J.; Nozaki, H.; Månsson, M.; Prša, K.; Amato, A.; Isobe, M.; Ueda, Y. *Phys. Procedia* **2012**, *30*, 186.
- (90) Liu, S.; Akbashev, A. R.; Yang, X.; Liu, X.; Li, W.; Zhao, L.; Li, X.; Couzis, A.; Han, M.-G.; Zhu, Y.; Krusin-Elbaum, L.; Li, J.; Huang, L.; Billinge, S. J. L.; Spanier, J. E.; O'Brien, S. *Sci. Rep.* **2014**, *4*, 6203.